King Saud University

Arabian Journal of Chemistry

www.ksu.edu.sa
www.sciencedirect.com

ORIGINAL ARTICLE

Sonochemical synthesis and characterization of $Mn^{2+}Mn_6^{3+}[SiO_4]O_8$ nanostructures and their application as photocatalyst for degradation of water-soluble organic pollutants below simulated sunlight

Zainab Hashim Khudhair [a], Masoud Hosseini [b], Mojgan Ghanbari [b], Makarim A. Mahdi [c], Layth S. Jasim [c], Masoud Salavati-Niasari [b],*

[a] *Department of Chemistry, College of Sciences for Women, Babylon University, Hilla, Iraq*
[b] *Institute of Nano Science and Nano Technology, University of Kashan, Kashan, P. O. Box. 87317-51167, Iran*
[c] *Department of Chemistry, College of Education, University of Al-Qadisiyah, Diwaniyah, Iraq*

Abstract In the present study, novel $Mn^{2+}Mn_6^{3+}[SiO_4]O_8$ (braunite, MSO) nanostructures were fabricated by a simple and affordable sonochemical method. The uniformity, structure, shape, and size of the product are affected by sonication time and power. $Mn^{2+}Mn_6^{3+}[SiO_4]O_8$ were used as a photocatalyst in the visible region due to their suitable bandgap (2.52 eV). The photocatalytic tests indicate that $Mn^{2+}Mn_6^{3+}[SiO_4]O_8$ nanostructures can degrade organic dyes, such as Eriochrome Black T (EBT) and Erythrosine (ER) in high values. Therefore, the degradation rate is 94.8% under ideal circumstances, which include 70 mg of catalyst and 10 ppm EBT. According to the kinetics study, the superior rate constant ($k = 0.0217\,min^{-1}$) results in the maximum photocatalytic efficiency (94.8%). The recycle test unveils that $Mn^{2+}Mn_6^{3+}[SiO_4]O_8$ is so stable and after five cycles, the photocatalyst efficiency decreased by 14.9 and 14.2% for EBT and erythrosine, respectively. Superoxide radicals were found to be the most active radicals implicated in the degradation of EBT and erythrosine by the scavenger's test.

---

* Corresponding author.
E-mail address: Salavati@kashanu.ac.ir (M. Salavati-Niasari).

ELSEVIER | **Production and hosting by Elsevier**

1. Introduction

Environmental contamination is significant as a result of the ubiquitous use of toxic coloring agents in industrial waste from the textile, paper, and garment sectors (Caglayan et al., 2019; Chiu et al., 2019; Kocyigit et al., 2018; Kucuk & Gulcin, 2016). According to several studies, the textile sector employs 10–12% of dyes yearly, with a significant amount (20%) wasted during fabrication and operating procedures and leads to effluent (Kumar & Pandey, 2017). These dyes include Rhodamine B, Methylene Blue (MB), Victoria blue, Red 120, Thymol blue Rose Bengal, Carmine, Indigo Red, and Eriochrome Black-T (EBT) (Deng et al., 2013; Wang et al., 2008; Xu et al., 2010). These dye-contaminated sewages contain toxic and nonbiodegradable colored pigments (Chen et al., 2010; Wang et al., 2021). Dye pollution affects aquatic environments even at very low concentrations (< 1 ppm) (Balarabe et al., 2022; Haider et al., 2022; Wahab et al., 2019). Therefore, it is crucial to remove dyes from wastewater (Sanakousar et al., 2022).

In recent years, it has become difficult to remove coloring agents and other contaminants from water (Naseem et al., 2018). In order to address this specific issue, a number of techniques have been used, including membrane biosorption (Hai et al., 2008; Wenten et al., 2020), filtration (Li et al., 2018), ozonation (Aziz et al., 2018), adsorption (Wazir et al., 2020; Zhou et al., 2019), biological/aerobic treatment (H. Zhang et al., 2018), ion exchange removal (Bashir et al., 2019; Feng et al., 2019), catalytic reduction (Khan et al., 2022; Sherin et al., 2020), coagulation (He et al., 2021), and photocatalytic degradation (Rafiq et al., 2021; Wu et al., 2020). The absorption method is typically preferred in terms of pre-release disposal procedures because of its simplicity of use and affordable cost (Guan et al., 2019). However, drawbacks, such as weak mechanical stability of adsorbents, low absorption effectiveness, and incomplete pollution removal, make it difficult to remove pollutants effectively (Ikram, Tabassum, et al., 2020; Raza et al., 2020).

Photodegradation of contaminants has gained enormous popularity in recent years (Gautam et al., 2020; Zhuang et al., 2022). A semiconductor photocatalyst absorbs sunlight to break down different ecological contaminants, including aquatic and atmospheric organic contaminants, in the photocatalytic reaction, which uses heterogeneous catalysis (Guo et al., 2021; Şendal et al., 2022). There are benefits to comparing photodegradation to more conventional wastewater treatment techniques. For example, active photocatalysts at ambient temperature can totally break down toxic pollutants in a few hours. Furthermore, toxic pollutants can be thoroughly processed to yield relatively safe byproducts (CO_2 and water) without producing any additional toxic byproducts (Maruthapandi et al., 2021). Nanomaterials' surface functionalization is used in photodegradation to efficiently remove dangerous contaminants (Ikram, Hassan, et al., 2020; Nguyen et al., 2021). Multiple functional factors, including reaction temperature, irradiation intensity, pH of the solution, and initial dye concentration, influence the entire photodegradation procedure, from dye molecule adsorption on the photocatalyst surface to dye molecule decomposition by reactive radicals (Abkar et al., 2021; Ghanbari & Salavati-Niasari, 2021; Karami et al., 2021).

In recent years, there has been a growing interest in the development of nanostructure-based photocatalysts for the degradation of organic pollutants or toxic molecules. These materials have shown great potential for environmental remediation due to their high surface area, unique electronic and optical properties, and efficient charge separation (Yang et al., 2023). Several recent studies have focused on the development and application of nanostructure-based photocatalysts for the degradation of organic pollutants and toxic molecules. One recent study by Liu et al. reported the synthesis of a novel $ZnO@TiO_2$ core–shell nanorod photocatalyst for the degradation of bisphenol A (BPA). The results showed that the $ZnO@TiO_2$ nanorods exhibited enhanced photocatalytic activity compared to pure TiO_2 nanoparticles, attributed to the efficient charge transfer between ZnO and TiO_2 (Liu

et al., 2020). Furthermore, Zhang et al.synthesized a novel $Ag_3PO_4/$AgBr binary composite photocatalyst for the degradation of rhodamine B under visible light irradiation. The results showed that the ternary composite exhibited significantly enhanced photocatalytic activity compared to single-component photocatalysts due to its synergistic effect (X. Zhang et al., 2018). Zhang et al. explored the use of graphene-based nanocomposites as efficient photocatalysts for the degradation of various organic dyes. The researchers synthesized a hybrid material consisting of graphene oxide and metal oxide nanoparticles, which exhibited excellent photocatalytic activity under visible light irradiation (Zhang et al., 2020). In another study conducted by Matos et al, titanium dioxide (TiO_2) nanoparticles were doped with carbon to enhance their photocatalytic performance. The researchers found that C-doped anatase TiO_2 efficiently degrade organic pollutants, including phenol and methylene blue dye (Matos et al., 2019). Additionally, carbon-based nanostructures have also been extensively studied for their photocatalytic properties. A recent study by Xiao et al. reported on the synthesis of carbon nitride nanosheets with enhanced visible light absorption capabilities for the degradation of organic pollutants. The researchers found that the carbon nitride nanosheets exhibited excellent photocatalytic activity and stability, making them promising candidates for environmental remediation applications (Xiao et al., 2021).

The ternary system Mn-Si-O has the three silicate phases Mn_2SiO_4, $MnSiO_3$, and Mn_7SiO_{12} at atmospheric pressure, which are represented by tephroite, minerals rhodonite, and braunite, respectively. The $Mn^{2+}Mn_6^{3+}[SiO_4]O_8$ phase, also known as $MnSiO_3.3Mn_2O_3$, is composed of di- and trivalent manganese. These minerals, particularly $Mn^{2+}Mn_6^{3+}[SiO_4]O_8$, are significant components of manganese rocks and ores. Tephroite and rhodonite are also interesting to metal workers (Huang & Rosén, 1994). $Mn^{2+}Mn_6^{3+}[SiO_4]O_8$ with the chemical formula of $Mn^{2+}Mn_6^{3+}[SiO_4]O_8$ has a brownish-black appearance (De Villiers, 1980). The commercial importance of manganese ore processing and the producing of manganese compounds and alloys cannot be overstated. The chemical and metallurgical industries heavily rely on manganese (Mn), one of the less common elements on earth (Yartasi et al., 1997). Some potential advantages of MSO nanostructures could include: Magnetic properties: Manganese is a magnetic element, and the presence of both Mn^{2+} and Mn^{3+} ions in the nanostructure could result in interesting magnetic properties that could be useful for various applications. Optical properties: Silicate materials are known for their optical properties, and the addition of manganese ions could enhance these properties further. This could make MSO nanostructures useful for applications such as optoelectronics. Catalytic activity: Manganese is also known to have catalytic activity, and the presence of manganese ions in the nanostructure could enhance this property. This could make MSO nanostructures useful for catalytic applications. Biocompatibility: Silicate materials are generally biocompatible, meaning they are not harmful to living cells or tissues. Overall, more research is needed to fully understand the potential advantages of $Mn^{2+}Mn_6^{3+}[SiO_4]O_8$ nanostructures and their practical applications.

In this work, we aim to fabricated and characterize $Mn^{2+}Mn_6^{3+}[SiO_4]O_8$ nanostructures using a simple and fast sonochemical approach. This is the first time that this compound was prepared by ultrasound radiation and its photocatalytic behavior was studied through different organic dyes under visible radiation.

2. Materials and methods

2.1. Materials

Manganese (II) nitrate tetrahydrate 98% ($Mn(NO_3)_2 \cdot 4H_2O$), Tetraethyl orthosilicate > 99% (TEOS), Tetraethylenepentamine > 95% (TEPA), Eriochrome Black-T (EBT), Erythrosine, Ethylenediaminetetraacetic acid (EDTA), Benzoic

acid (BA), and 1,4-Benzoquinone (BQ), were acquired from Sigma-Aldrich and applied with no additional purification.
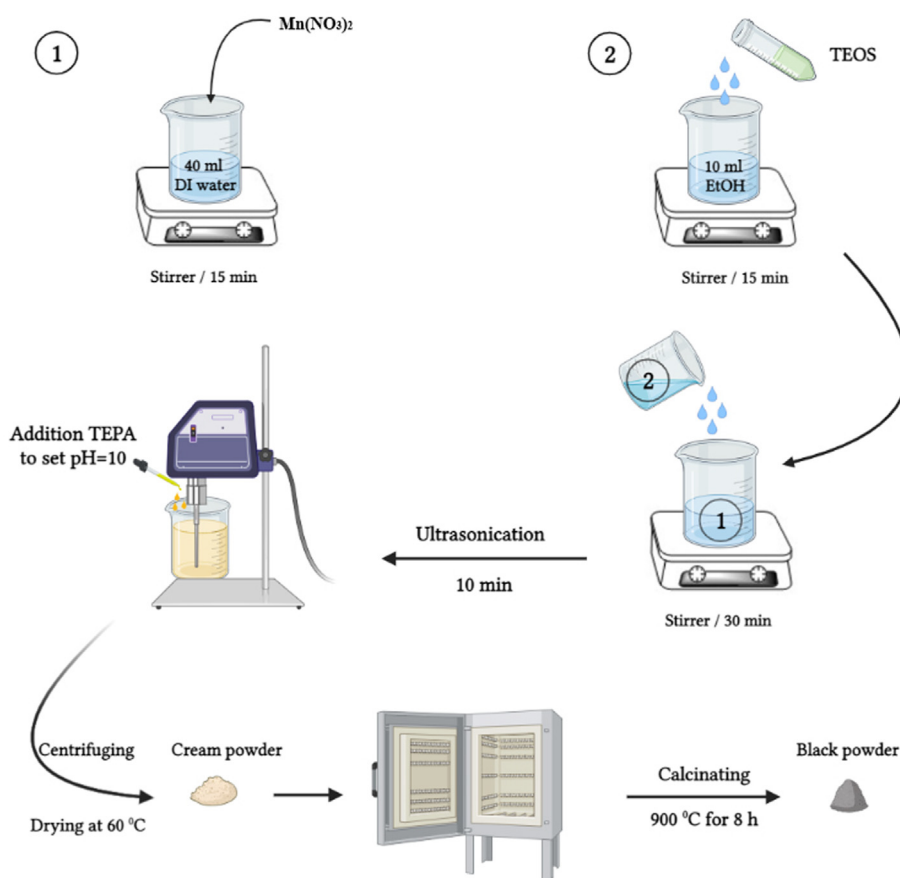
2.2. Preparation of $Mn^{2+}Mn^{3+}_6[SiO_4]O_8$ nanostructures

810 mg of $Mn(NO_3)_2$ was liquefied in 40 mL of distilled water and mixed for 10 min (solution A). Then, 360 μl of TEOS and 10 mL of ethanol were combined and agitated for 15 min (solution B). The solution B was mixed with solution A under ultrasonic radiation. TEPA was added to the mixture to adjust the pH of the solution to 10. The precipitate was rinsed several times with ethyl alcohol and dried at 70 ℃ for 12 h. Finally, the powder was calcined at 900 ℃ for 8 h. The sonication time and power were varied (Table 1 and Scheme 1) to obtain the best product.

2.3. Photocatalytic behavior

Investigation of the photocatalytic application of Mn^{2+}-$Mn^{3+}_6[SiO_4]O_8$ nanostructures was performed over eriochrome Black-T and erythrosine. A typical procedure involved mixing 50 mL of dye with various braunite contents and stirring it in the dark for 0.5 h. Then, an Osram 400 W visible light (containing a wavelength in the range of 400 to 780 nm) was turned on. The solution containing dye was aerated continuously to supply O_2. At specific time intervals, 3 mL of the dye was removed, centrifuged to remove the $Mn^{2+}Mn^{3+}_6[SiO_4]O_8$, and scrutinized with a UV–Vis spectrometer. The degradation rate (D) was calculated as (Ghanbari & Salavati-Niasari, 2021):

Table 1 Different conditions for fabrication of $Mn^{2+}Mn^{3+}_6[SiO_4]O_8$.

Sample No.	Time of sonication (min)	Power of sonication (W)	Grain size (nm) from Scherrer formula (Abkar et al., 2021)	Calcination temperature (℃)	Calcination time (h)
1	5	40	18.9	900	8
2	7	40	42.9		
3	10	40	26.4		
4	5	60	–		
5	5	80	–		

Scheme 1 Schematic of fabrication process of $Mn^{2+}Mn^{3+}_6[SiO_4]O_8$ by sonochemical method.

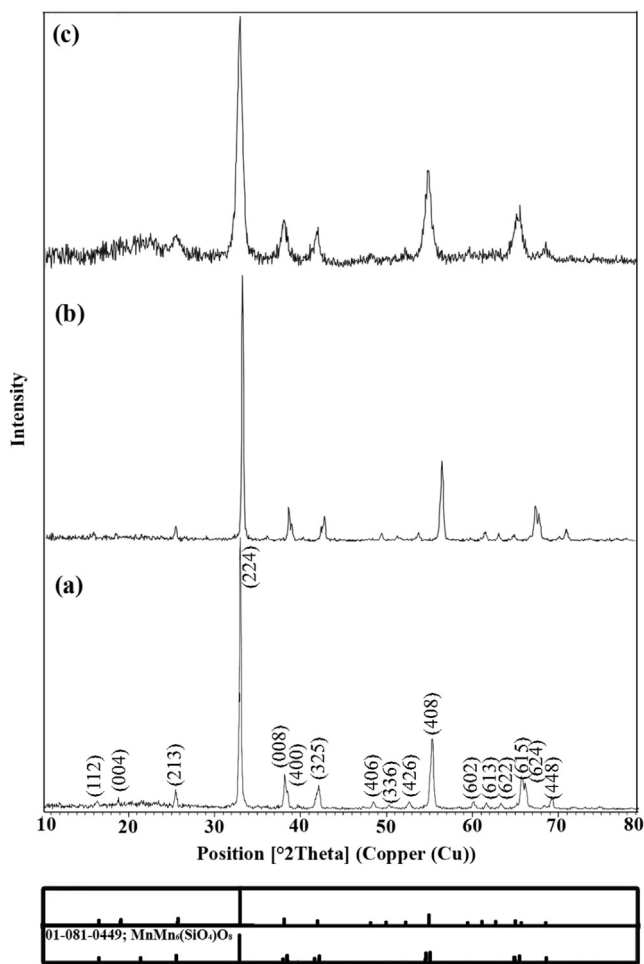**Fig. 1**   XRD patterns of $Mn^{2+}Mn_6^{3+}[SiO_4]O_8$ in three different times of sonication a) 5 min, b) 7 min, and c) 10 min.

$$D = \frac{A_0 - A_t}{A_0} \times 100 \qquad (1)$$

So that, A_0 and A_t display the initial absorption and absorption at specific time (t), respectively.
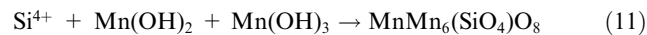
2.4. Physical instruments

XRD patterns were registered to utilize an X-ray diffractogram (Philips) among X' Pert Pro sieved through copper K_α irradiation ($\lambda = 15.4$ nm). FT-IR spectra of nanomaterials the samples were recorded by a Shimadzu Varian 4300 spectrophotometer in KBr pellets in the range of 400 to 4000 cm^{-1}. The element examination from the samples was registered using the EDS analysis device with 20 kV stimulating charge. The tiny structure of the outcomes were procured over a ZEISS field emission scanning electron microscopy. Before catching images, the products were coated by a thin transparent coating of gold to avoid charge accretion and create the product exterior conductive, and achieving a greater dissimilarity. GC-2550TG (Teif Gostar Faraz Company, Iran) were used toward all chemical agents. The surface areas (BET) were defined through N_2 adsorption at $-196\,°C$ using an automatic gas adsorption analysis device (Tristar 3000,

Micromeritics). Diffuse reflectance UV–vis spectroscopy was performed with a Shimadzu UV/3101 PC ranging from 200 and 800 nm. An MPI Ultrasonic; welding, 1000 W, 20 kHz, Switzerland (multi-wave ultrasound generator) was provided by a transducer/converter. A titanium oscillator was utilized for the ultrasound radiation. Transmission electron microscope (TEM) was carried out employing a TEM Philips EM208 with an accelerating voltage of 100 kV.

3. Results and discussion

3.1. Characterization

The XRD patterns of $Mn^{2+}Mn_6^{3+}[SiO_4]O_8$ fabricated by sonochemical method in three various sonication times, including 5, 7 min, and 10 min are illustrated in Fig. 1. These patterns show that in three different sonication times, $MnMn_6(SiO_4)O_8$ with reference code of 01–081-0449 and tetragonal structure (Space group = I41/acd) is formed (Haghjoo, Sangsefidi, Hashemizadeh, et al., 2017). The production of $MnMn_6(SiO_4)O_8$ nanoparticles is accomplished by ultrasound. Cavitation caused by ultrasonic waves is used to make suitable nanoscale structures. Hot-spot theory postulates that high energies are used to produce extreme temperatures and tensions, which in turn produce active species of radicals (Dheyab et al., 2020). The following reactions show how the sonochemical process is being used to fabricate the product:

$$H_2O \rightarrow \bullet H + \bullet OH \qquad (2)$$

$$2\bullet OH \rightarrow H_2O_2 \qquad (3)$$

$$2\bullet H \rightarrow H_2 \qquad (4)$$

$$O_2 + \bullet H \rightarrow \bullet O_2H \qquad (5)$$

$$\bullet O_2H + \bullet H \rightarrow H_2O_2 \qquad (6)$$

$$2\bullet O_2H \rightarrow H_2O_2 + O_2 \qquad (7)$$

$$H_2O + C_8H_{23}N_5 + \bullet H \rightarrow OH^- + C_8H_{23}N_5\text{-}H^+ \qquad (8)$$

$$Mn(NO_3)_2 + 2OH^- \rightarrow Mn(OH)_2 + 2NO_3^- \qquad (9)$$

$$O_2 + Mn(OH)_2 + H_2O \rightarrow Mn(OH)_3 \qquad (10)$$

$$Si^{4+} + Mn(OH)_2 + Mn(OH)_3 \rightarrow MnMn_6(SiO_4)O_8 \qquad (11)$$

The elemental composition of products is investigated using energy-dispersive X-ray spectroscopy (EDS). The sample's EDS results demonstrate the presence of oxygen, silicon, and manganese elements, with no impurities observed (Fig. 2).

Fig. 2f illustrates the FT-IR spectrum of $Mn^{2+}Mn_6^{3+}[SiO_4]O_8$ nanostructures. The absorption peaks at 1637 cm^{-1} and 3431 cm^{-1} are related to the bending vibration of H-O–H and the O–H bond stretching vibration, respectively, due to the moisture absorption. The characteristic bands associated with Mn-O bond vibrations are primarily seen in two locations: a doublet (Mn-O-Mn) at 473 cm^{-1} and a primary and an intense peak at 637 cm^{-1} (Haghjoo, Sangsefidi, Hashemizadeh, et al., 2017). The absorption bands located at
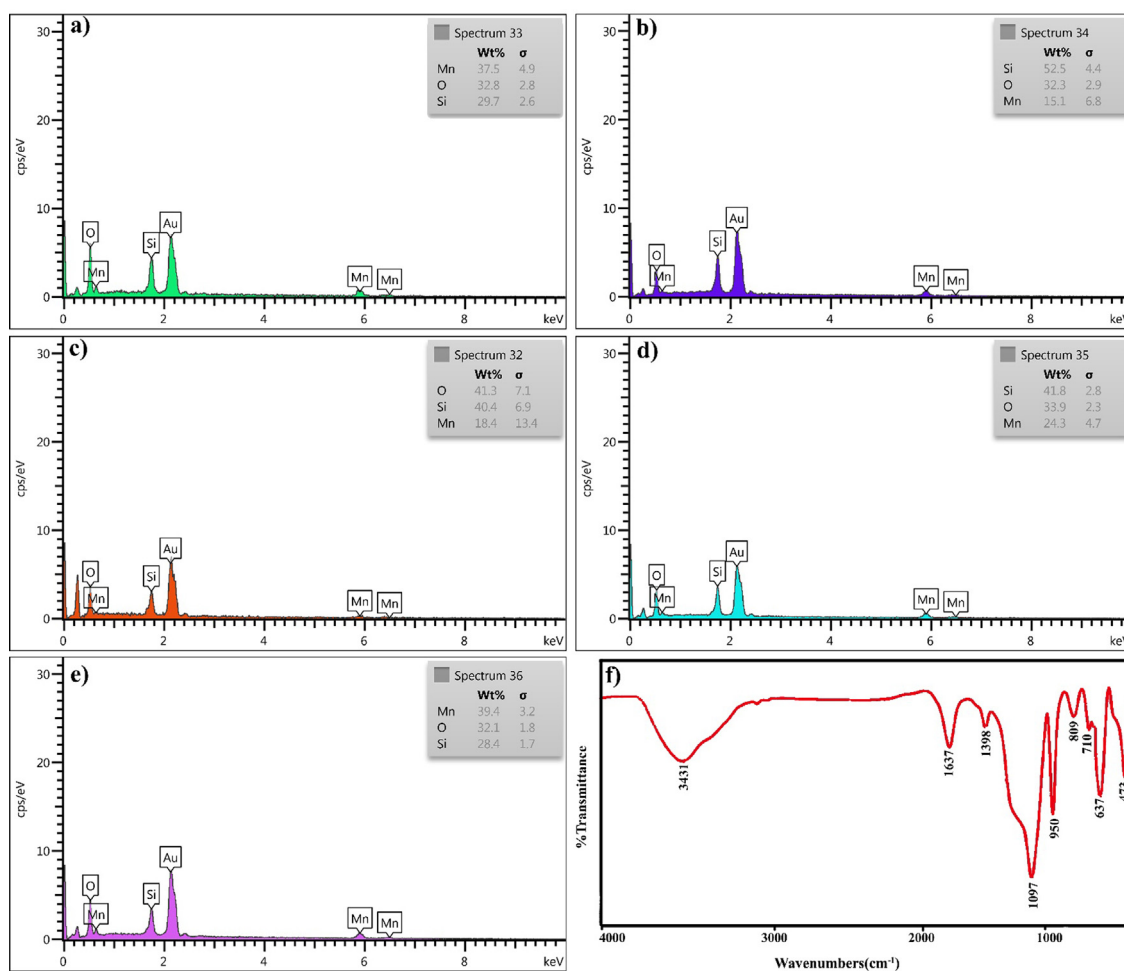
Fig. 2 EDS spectra of $Mn^{2+}Mn^{3+}_6[SiO_4]O_8$ in different condition, a) 5 min and 40 W, b) 7 min and 40 W, c) 10 min and 40 W, d) 5 min and 60 W, e) 5 min and 80 W, and f) FTIR spectra of $Mn^{2+}Mn^{3+}_6[SiO_4]O_8$ nanostructures prepared in the presence of 5 min and 40 W sonication.

1097 cm^{-1} and 950 cm^{-1} are because of the formation of O-Si-O and Si-O-Mn groups, respectively (Ionescu et al., 2010).

The impact of time and power of sonication was studied on the shape of $Mn^{2+}Mn^{3+}_6[SiO_4]O_8$ nanostructures using FESEM images. Fig. 3 reveals the morphology of Mn^{2+}-$Mn^{3+}_6[SiO_4]O_8$ nanostructures in three different sonication times. As can be seen, agglomeration is increased by enhancing sonication time due to increasing the temperature of reaction. When the ultrasound wave is emitted for a longer period of time, the temperature of the solution rises, causing the product particles to grow larger (Ghanbari & Salavati-Niasari, 2018). Considering that the sonication time has no effect on the purity and structure of the composition, the irradiation time of 5 min was chosen as the optimal time. Furthermore, Fig. 4 displays the influence of sonication power on the shape of Mn^{2+}-$Mn^{3+}_6[SiO_4]O_8$ nanostructures. As observed, increasing the sonication power leads to large particles as the temperature rises. As a result, the optimum sonication power and time were chosen to be 40 W and 5 min, respectively. The TEM images of $Mn^{2+}Mn^{3+}_6[SiO_4]O_8$ nanostructures prepared at the optimal condition (5 min and 40 W) are manifested in Fig. 5. These images show the uniform nanoparticles, which have an average size of 40 nm are observed in.

The Brunauer-Emmett-Teller surface area (BET) analysis measured N_2 adsorption (ADS)/desorption (DES) at 77 k. N_2 ADS/DES isotherm and pore size distribution plots are exhibited in Fig. 6a and 6b, respectively. Based on the IUPAC category, the isotherm is classified as an IV-type isotherm with H3 hysteresis. The specific surface area of $Mn^{2+}Mn^{3+}_6[SiO_4]O_8$ nanostructures is calculated at 23.595 m^2/g. The pore volume and pore diameter of $Mn^{2+}Mn^{3+}_6[SiO_4]O_8$ nanostructures distinguished from the BJH plot are 0.041211 cm^3/g and 6.9863 nm, which implies $Mn^{2+}Mn^{3+}_6[SiO_4]O_8$ mesoporous structures.

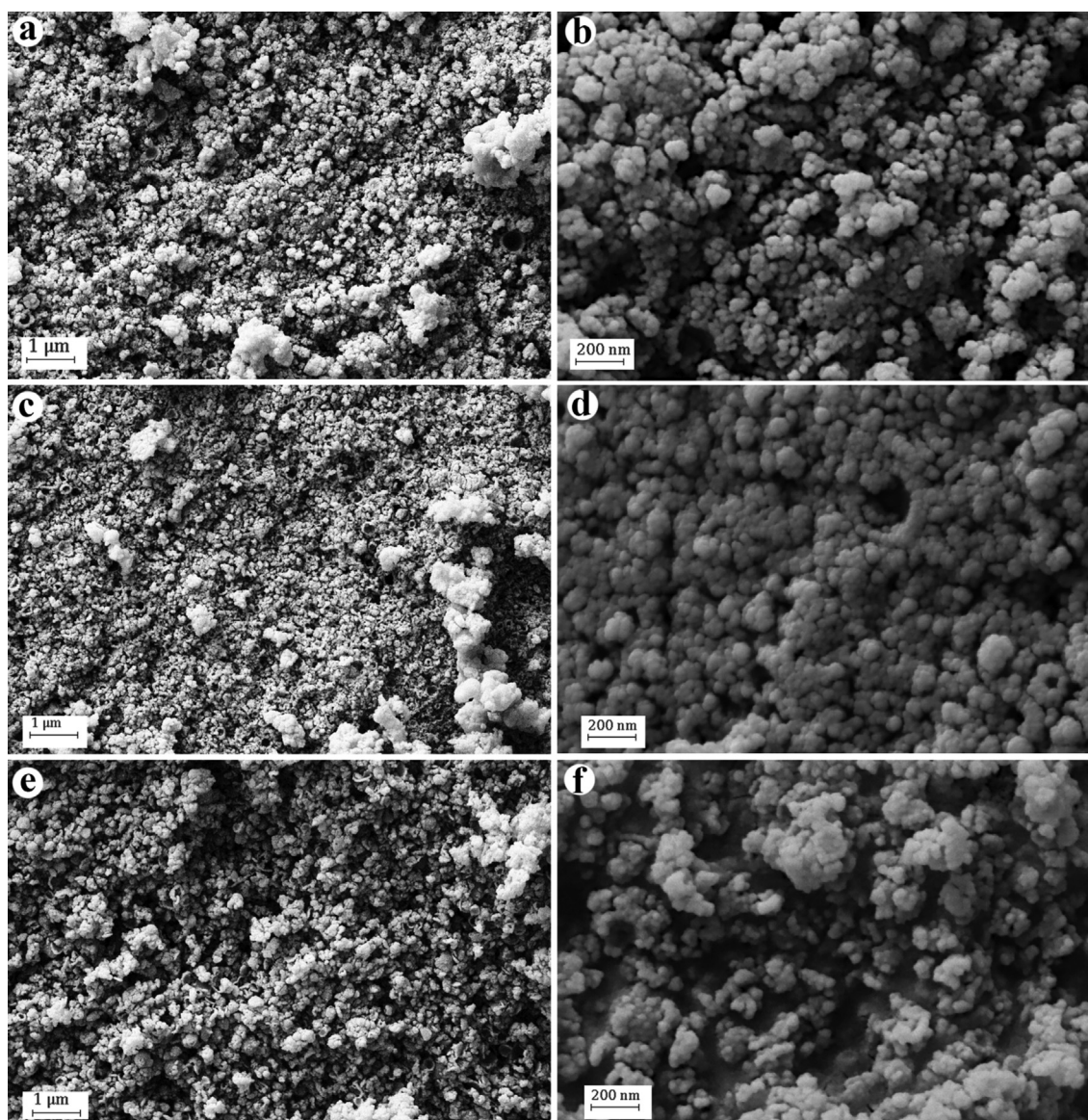The optical absorption of $Mn^{2+}Mn^{3+}_6[SiO_4]O_8$ nanostructures is investigated using diffuse reflectance spectroscopy

Fig. 3 FESEM images of $Mn^{2+}Mn_6^{3+}[SiO_4]O_8$ in three different sonication times (a and b) 5 min, (c and d) 7 min, and (e and f) 10 min with 40 W sonication power.

(DRS). The optical bandgap energy is determined by the absorbance energy and photon, which was calculated using Tauc method utilizing the following equation:

$$A(h\upsilon - B.G.) = (\alpha h\upsilon)^n \tag{12}$$

Where υ, α, h, A, and B.G. are the frequency, absorbance, Planck constant, material constant, and optical bandgap, respectively. Fig. 6c illustrates the absorption spectrum of $Mn^{2+}Mn_6^{3+}[SiO_4]O_8$ nanostructures. The energy bandgap of the sample is calculated at 2.52 eV by linear extrapolation of $(\alpha h\upsilon)^2$ versus $h\upsilon$ to zero (Fig. 6d).

Magnetization behavior of $Mn^{2+}Mn_6^{3+}[SiO_4]O_8$ was measured using a vibrating sample magnetometer (VSM) at 300 k (Fig. 6e). $Mn^{2+}Mn_6^{3+}[SiO_4]O_8$ nanostructures display a superparamagnetic behavior. The maximum saturation magnetization is about 0.906 emu/g. The magnetic properties of materials make it possible to utilize them as a new catalyst

to remove dyes from aqueous media and magnetically collect the catalyst.

3.2. Photocatalytic activity

The behavior of $Mn^{2+}Mn_6^{3+}[SiO_4]O_8$ nanostructures was studied over the decolorization of erythrosine (ER) and eriochrome black-T (EBT) under visible radiation (Scheme 2). The degradation percentages of ER and EBT are 77.5% and 88.8%, respectively (Fig. 7a). One of the significant factors in degradation efficiency is catalyst dosage. Increasing the catalyst dosage can enhance the photocatalytic efficiency due to increasing the surface (Rahimzade et al., 2021). Fig. 7c unveils the effect of $Mn^{2+}Mn_6^{3+}[SiO_4]O_8$ content (30, 50, and 70 mg) on the degradation of eriochrome black-T. Therefore, the degradation performance is improved by increasing the
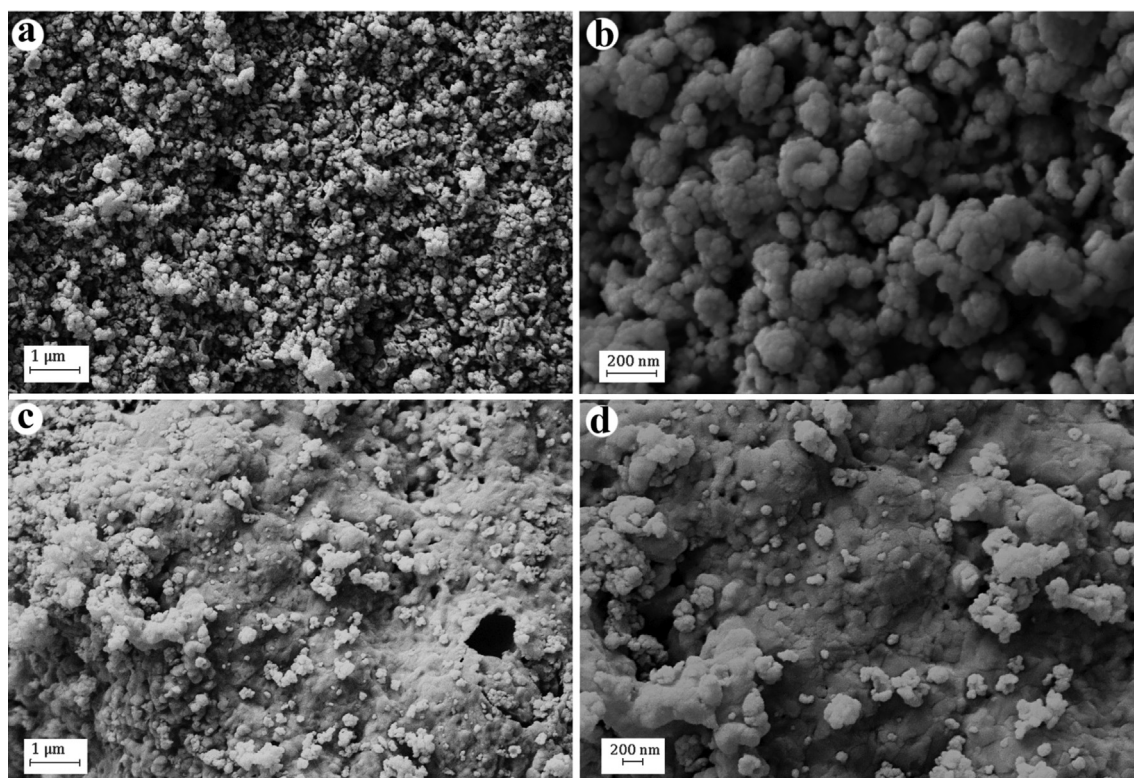
Fig. 4 FESEM images of $Mn^{2+}Mn^{3+}_6[SiO_4]O_8$ in two different sonication powers (a and b) 60 W, and (c and d) 80 W at 5 min sonication time.

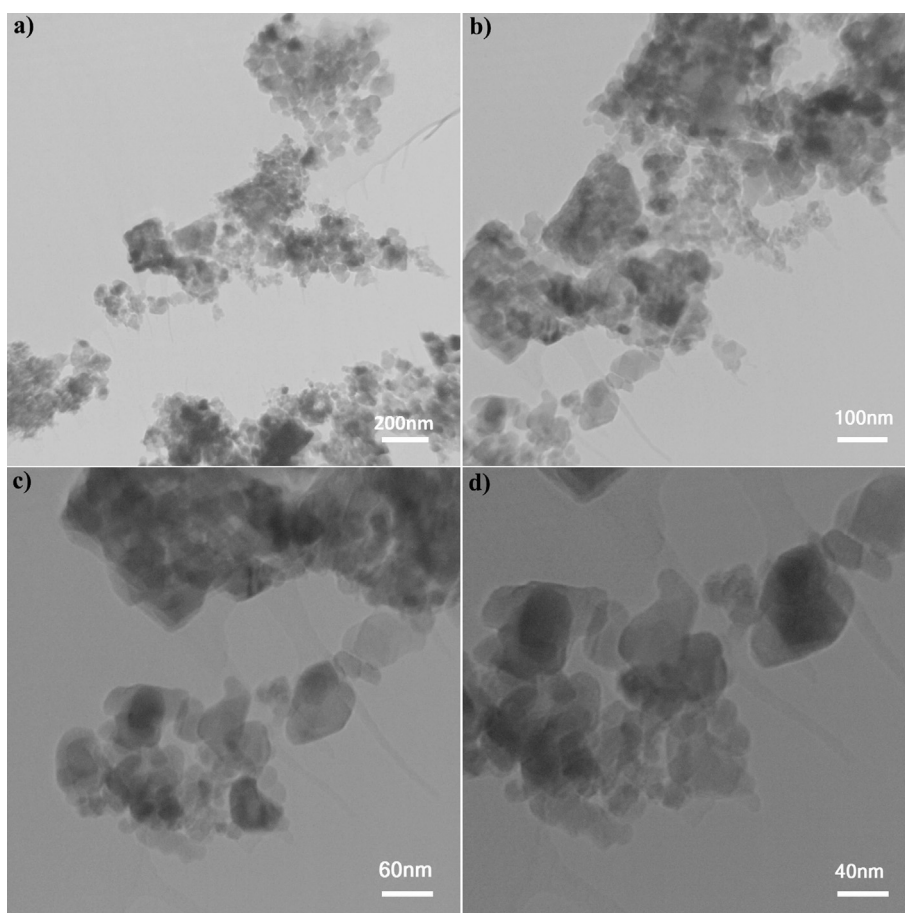**Fig. 5** TEM images of $Mn^{2+}Mn^{3+}_6[SiO_4]O_8$ prepared in the presence of 5 min and 40 W sonication.

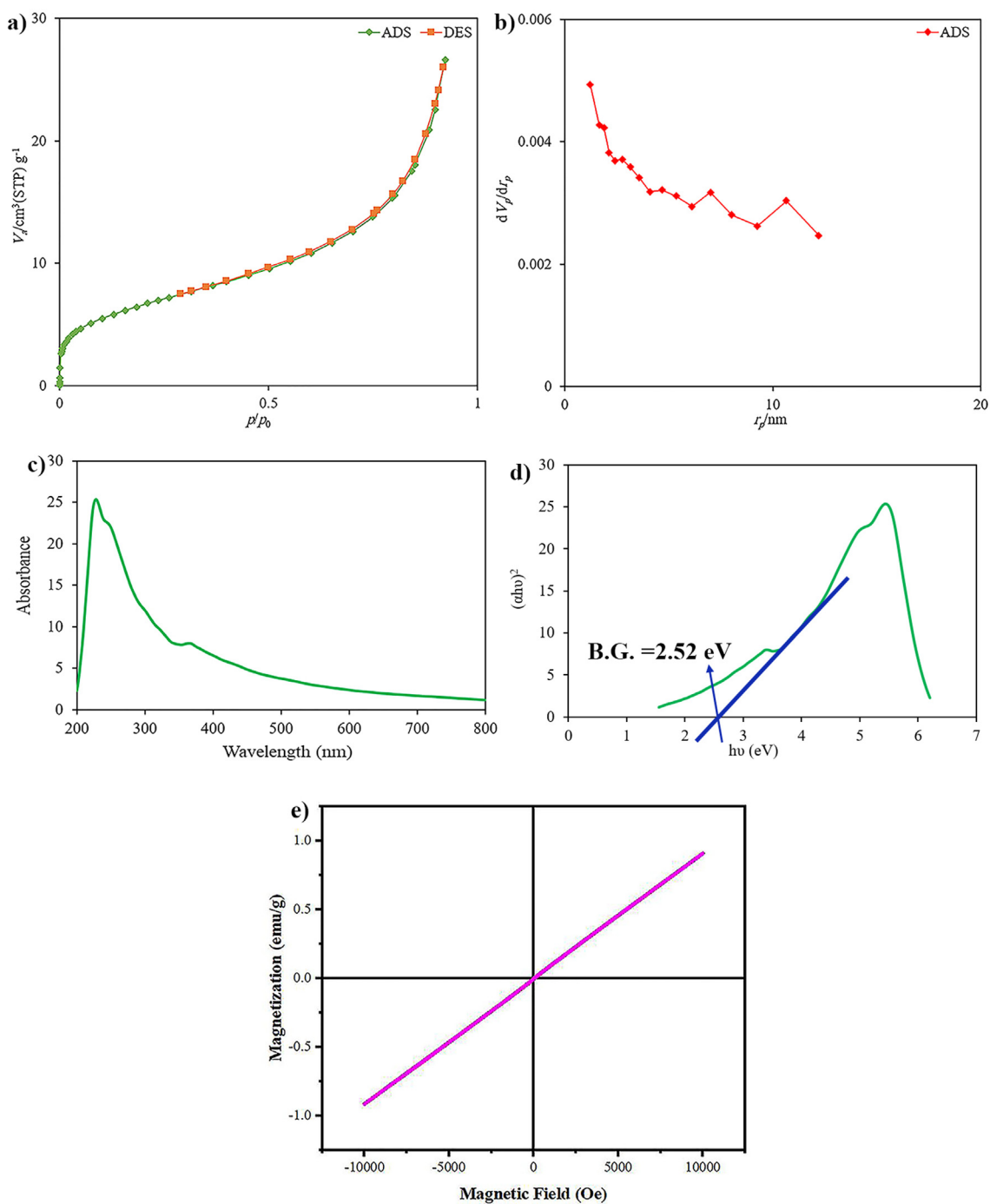**Fig. 6** A) ads-des isotherm, b) bjh plot, c) drs spectrum, d) tauc plot, and e) vsm diagram of $mn^{2+}Mn_6^{3+}[SiO_4]O_8$ at 5 min and 40 W sonication time and power.

amount of $Mn^{2+}Mn_6^{3+}[SiO_4]O_8$. As a result, the degradation percentages for 30, 50, and 70 mg $Mn^{2+}Mn_6^{3+}[SiO_4]O_8$ are 82.2%, 88.8%, and 94.8%, respectively. The concentration of organic dyes is another major aspect in their degradation. The catalyst's efficiency decreases as pollutant concentration rises (Wang et al., 2022). As illustrated in Fig. 7e, eriochrome black-T degradation was decreased by increasing its concentration. So, 70 mg $Mn^{2+}Mn_6^{3+}[SiO_4]O_8$ nanostructure degraded 94.8%, 91.3%, and 84.8% of 10 ppm, 15 ppm, and 20 ppm of eriochrome black-T. The photocatalytic efficiency decreases

with the increase in pollutant concentration because when there are more pollutants present, they compete for the available active sites on the photocatalyst surface. This reduces the number of reactive species that can be generated and decreases the overall efficiency of the process. Additionally, at higher pollutant concentrations, there may be a saturation effect where all available active sites are already occupied, and further pollutant molecules cannot be adsorbed or degraded efficiently. Furthermore, the Langmuir-Hinshelwood reaction was
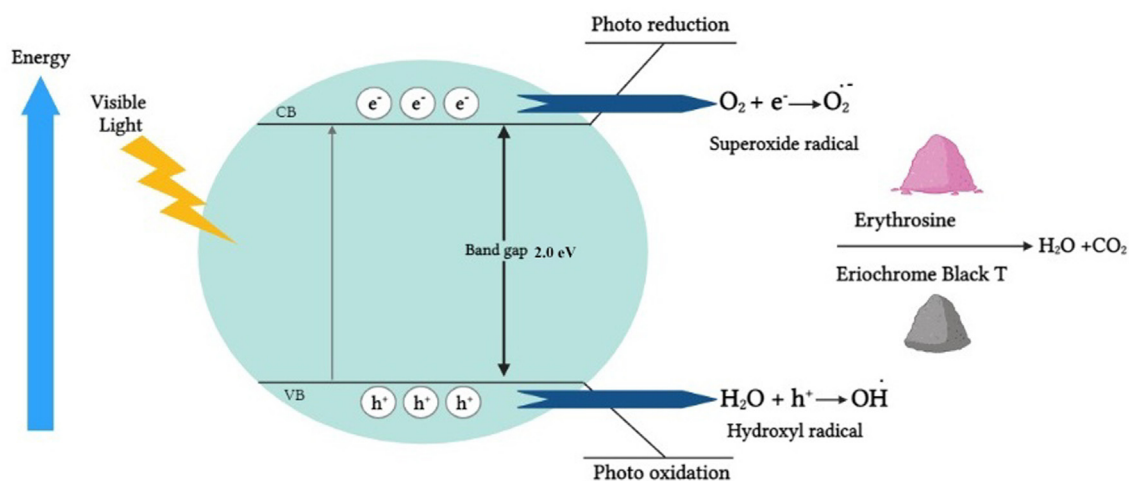
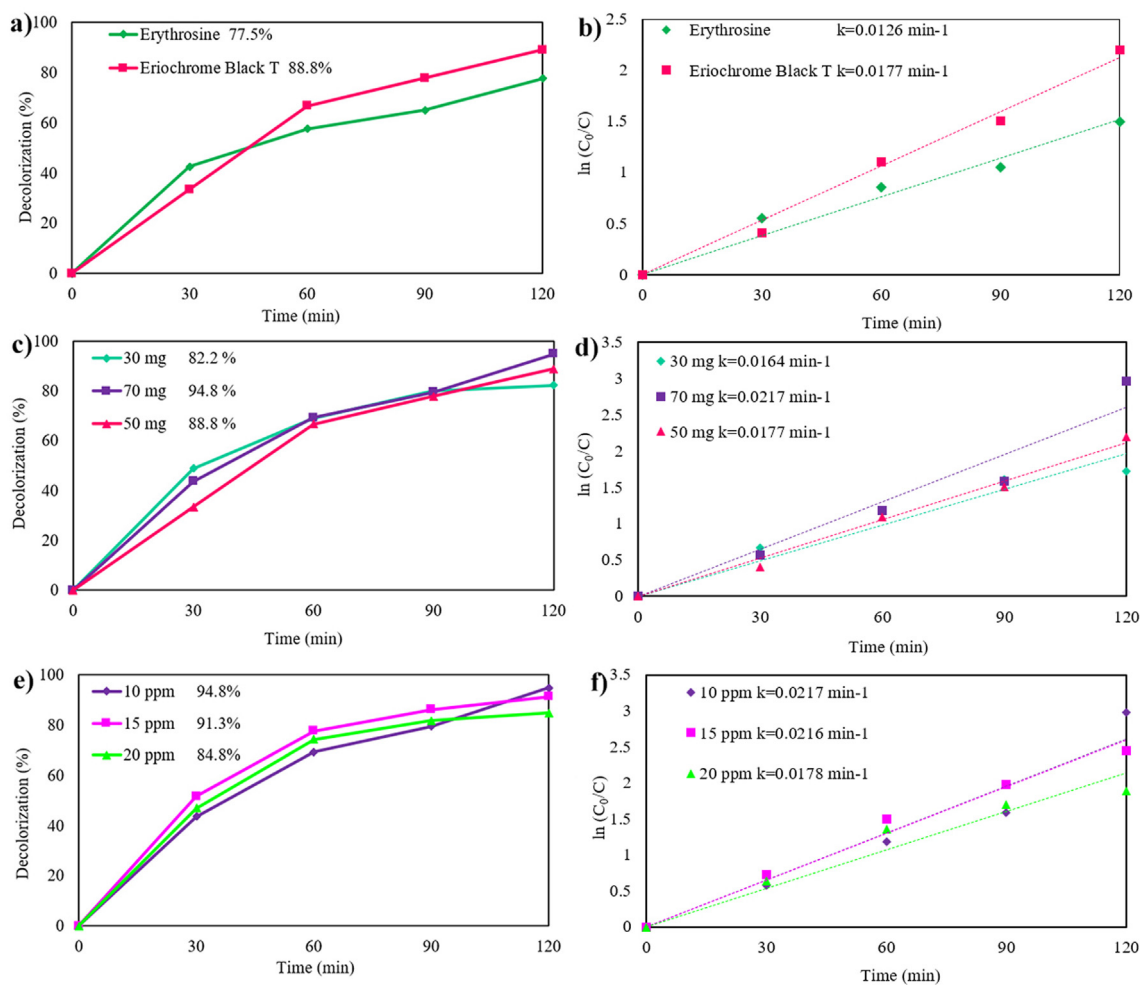**Scheme 2**   Schematic of photocatalysis process in the presence of $Mn^{2+}Mn^{3+}_6[SiO_4]O_8$.

Fig. 7   Photocatalytic degradation and ln(C0/C) plots of (a and b) two different dyes with 10 ppm concentration, (c and d) various catalyst dosages over 10 ppm EBT, (e and f) different concentrations of EBT in the presence of 70 mg $Mn^{2+}Mn^{3+}_6[SiO_4]O_8$.

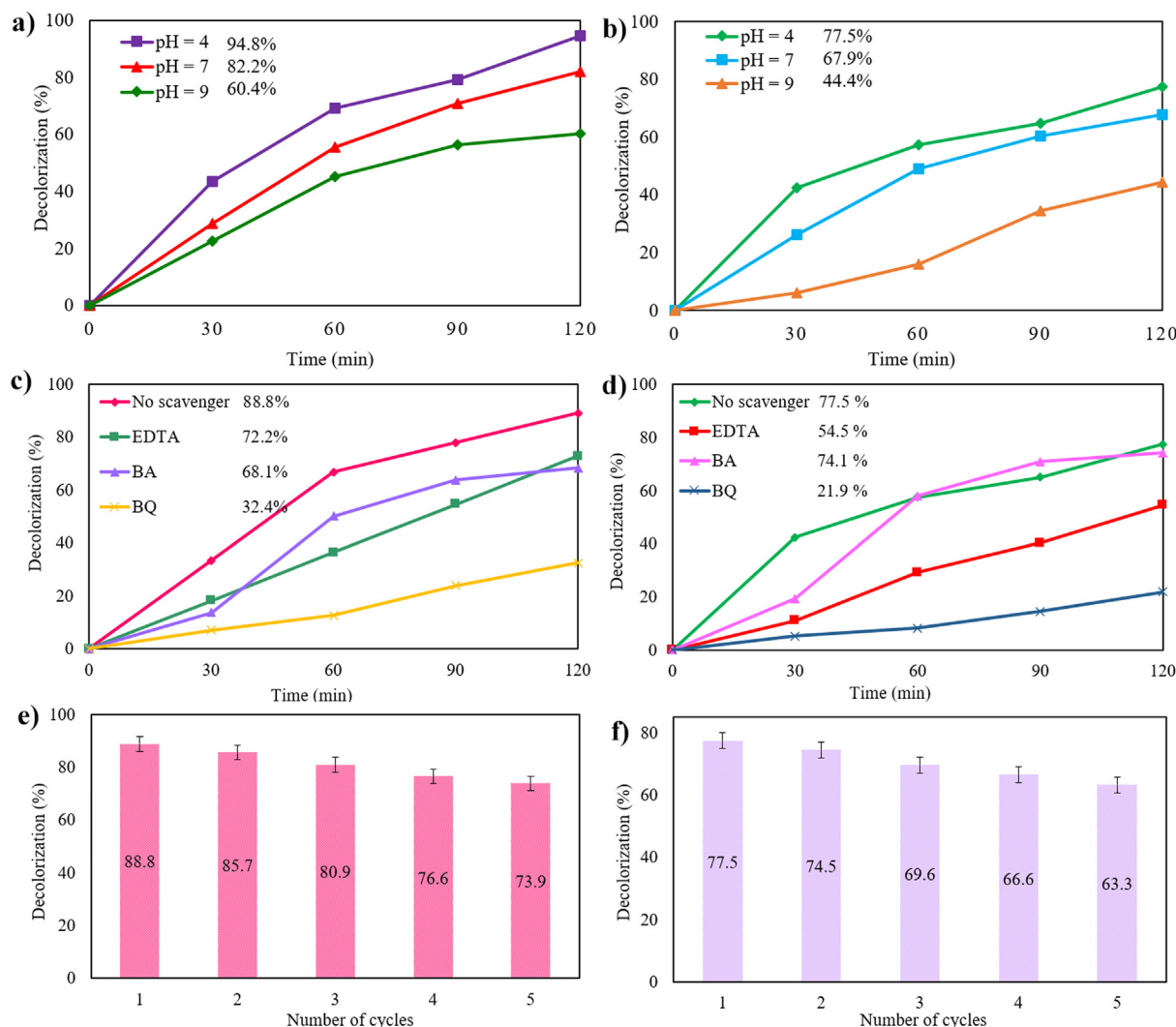**Fig. 8** Effect of different pH media, scavengers, and recyclability of $Mn^{2+}Mn_6^{3+}[SiO_4]O_8$ over (a, c, and e) EBT, (b, d, and f) erythrosine, respectively.

used to determine the possible reaction rate constant (k) (Ghanbari & Salavati-Niasari, 2021).

$$\ln\left(\frac{C_0}{C}\right) = kt \tag{13}$$

C_0 and C are the primary concentration, and concentration at t time, respectively. k is the Pseudo-first order rate constant (min^{-1}) and is determined by linear correlations between reaction time and $\ln(C_0/C)$. The highest performance is attained in a bigger reaction rate constant, as shown in Fig. 7b, 7d, and 7f. The effect of the pH of the solution was studied on the removal efficiency of EBT and ER (Fig. 8a and 8b). The degradation efficiency of EBT in acidic (pH = 4), neutral (pH = 7), and alkaline (pH = 9) media was about 94.8%, 82.2%, and 60.4%, respectively (Fig. 8a). Besides, the degradation rate of ER in acidic (pH = 4), neutral (pH = 7), and alkaline (pH = 9) media of EBT was about 77.5%, 67.9%, and 44.4%, respectively (Fig. 8b). These data demonstrated that the most increased efficiency was at acidic media (pH = 4). The catalyst's surface becomes positively charged at low pH levels, which can improve how well it interacts with dye mole-
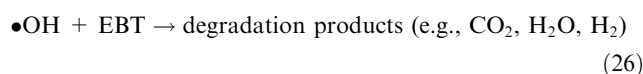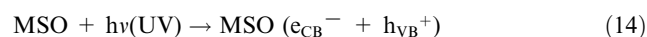
cules that are negatively charged. Higher degradation rates may occur as a result of greater dye molecule adsorption on the catalyst surface. On the other hand, the catalyst and dye molecules both acquire a negative charge at high pH levels. Lower degradation rates may result from less contact and adsorption between them (Yousefzadeh et al., 2022). Table 2 compared the photodegradation of different semiconductor compounds. As seen in this table, $Mn^{2+}Mn_6^{3+}[SiO_4]O_8$ can compete with other semiconductor photocatalysts. We can nominate $Mn^{2+}Mn_6^{3+}[SiO_4]O_8$ as a novel catalyst for the water purification process.

The active species were scrutinized to comprehend the mechanism of the photocatalytic process. The most likely active species implicated in the photodegradation of organic pollutants are superoxide radical anion ($\bullet O_2^-$), holes (h^+), and hydroxyl radicals ($\bullet OH$) (Kadam et al., 2017). Benzoic acid (BA), EDTA, and 1,4-Benzoquinone (BQ) were introduced as scavengers for $\bullet OH$, h^+, and $\bullet O_2^-$, respectively, to determine which active species are more in charge of the degradation of EBT and erythrosine in the photocatalytic reaction. (Cui et al., 2021). Fig. 8c and 8d obviously demonstrate that

Table 2 Comparison of Photocatalytic performance of different silicate compounds.

Catalyst	Bandgap (eV)	Solution pH	Highest degradation (%)	Dye concentration (ppm)	Catalyst dosage (g/mL)	Source of light/ Time (min)	Ref.
MSO	2.52	4	94.8 (EBT)	10	0.007/50	visible/120	This work
Mg_2SiO_4	3.38	3	82 (Acid Brown)	20	0.005/200	UV/90	(Moshtaghi et al., 2021)
Co_2SiO_4	3.3	7	95 (Acid Brown)	10	0.04/40	UV/120	(Bayat et al., 2016)
$PbSiO_3$	3.38	7	100 (Reactive Red 120)	5	0.05/50	UV/80	(Haghjoo, Sangsefidi, & Salavati-Niasari, 2017)
$Ag_6Si_2O_7$	1.6	7	90 (Methylene Blue)	10	0.05/100	Vis/120	(Wang & Wu, 2021)
Pb_2SiO_4	3.3	7	52 (Reactive Orange16)	10	0.04/40	UV/75	(Haghjoo et al., 2018)
Mn_7SiO_{12}	3.15	8	89 (Methyl Violet)	5	0.05/50	UV/45	(Haghjoo, Sangsefidi, Hashemizadeh, et al., 2017)
$AgSiO/ Ag_2CO_3$	1.3	7	99 (Methylene Blue)	10	0.02/50	Vis/70	(Cao et al., 2017)
$Ag_2Si_2O_7/ CNT_s$	1.58	7	95 (Methylene Blue)	10	0.05/100	Vis/120	(Wang & Wu, 2021)

the highest photocatalytic degradation of EBT and erythrosine occurred without using a scavenger. Nevertheless, the generated active species would interact favorably with scavengers and prevent EBT and erythrosine from degrading through photosynthesis. When EDTA and BA are applied as a scavenger, the photodegradation of EBT and erythrosine is not significantly deteriorated. This phenomenon indicates that •OH and h^+ are not affecting the primary active species in the photocatalytic procedure. BQ significantly reduces degradation efficiency indicates that $•O_2^-$ was an active species. The scavenger tests reveal that $•O_2^-$ are the most radicals involve in the degradation of EBT and erythrosine. As indicated in Fig. 8e and 8f, the fabricated $Mn^{2+}Mn^{3+}_6[SiO_4]O_8$ nanostructures did not display a considerable loss in efficiency after five cycles. The degradation efficiency dropped from 88.8% to 73.9% for EBT and 77.5% to 63.3% after five cycles. Therefore, $Mn^{2+}Mn^{3+}_6[SiO_4]O_8$ revealed high recyclability.

The following is a description of the reactions that took place on the catalyst surface and led to the decolorization of EBT (Konstantinou & Albanis, 2004) (Scheme 2):

$$MSO + h\nu(UV) \rightarrow MSO\ (e_{CB}^- + h_{VB}^+) \tag{14}$$

$$MSO\ (h_{VB}^+) + H_2O \rightarrow MSO + H^+ + OH• \tag{15}$$

$$MSO\ (e_{CB}^-) + O_2 \rightarrow MSO + O_2•^- \tag{16}$$

$$2H^+ + •O_2^- \rightarrow H_2O_2 \tag{17}$$

$$H_2O_2 + e^- \rightarrow OH^- + •OH \tag{18}$$

$$h^+ + OH^- \rightarrow •OH \tag{19}$$

$$h^+ + H_2O \rightarrow H^+ + •OH \tag{20}$$

$$e^- + O_2 \rightarrow •O_2^- \tag{21}$$

$$O_2•^- + H^+ \rightarrow HO_2• \tag{22}$$

$$•O_2^- + H^+ + e^- \rightarrow HOO• \tag{23}$$

$$HOO• + H_2O \rightarrow •OH + H_2O_2 \tag{24}$$

$$h_{VB}^+ + EBT \rightarrow oxidation\ products \tag{25}$$

$$•OH + EBT \rightarrow degradation\ products\ (e.g.,\ CO_2, H_2O, H_2) \tag{26}$$

$$e_{CB}^- + EBT \rightarrow reduction\ products \tag{27}$$

Besides, the bandgap energy (B.G.) of a semiconductor can be calculated by the following equations (Salari & Kohantorabi, 2021; Salari & Zahiri, 2022)

$$E_{VB} = X - E^e + 0.5B.G. \tag{28}$$

$$E_{CB} = E_{VB} - B.G. \tag{29}$$

In which, X, E^e, and B.G. are the absolute electronegativity of the semiconductor, the free energy of electron in hydrogen scale (about 4.5 eV), and the bandgap energy, respectively. For $Mn^{2+}Mn^{3+}_6[SiO_4]O_8$, the values of X is 2.526 eV. The measured B.G. of $Mn^{2+}Mn^{3+}_6[SiO_4]O_8$ is 2.52 eV. The valence band, and conduction band energies are −0.713 eV, and −3.233 eV, respectively.

4. Conclusions

$Mn^{2+}Mn^{3+}_6[SiO_4]O_8$ were profitably fabricated time using a quick and low-cost sonochemical technique. The influence of sonication power and time of was evaluated on the uniformity, shape, structure, and size of $Mn^{2+}Mn^{3+}_6[SiO_4]O_8$ nanostructures. According to the DRS data, this compound has an appropriate bandgap (2.52 eV) in the visible region. The photocatalytic behavior of $Mn^{2+}Mn^{3+}_6[SiO_4]O_8$ nanostructures exhibited that this compound has high potential in the destruction of organic dyes, so, 70 mg $Mn^{2+}Mn^{3+}_6[SiO_4]O_8$ can degrade 94.8% of 10 ppm eriochrome black T under visible light. The kinetics study showed that a higher rate constant belongs to the

highest photocatalytic performance ($k = 0.0217\,min^{-1}$). The scavenger experiment indicated that superoxide radicals performed a major role in the photocatalysis process.

CRediT authorship contribution statement

Zainab Hashim Khudhair: Software, Methodology, Writing – review & editing. **Masoud Hosseini:** Software, Investigation, Methodology, Formal analysis. **Mojgan Ghanbari:** Data curation, Software, Writing – review & editing, Writing – original draft, Supervision. **Makarim A. Mahdi:** Software, Writing – review & editing. **Layth S. Jasim:** Software, Data curation, Validation. **Masoud Salavati-Niasari:** Software, Formal analysis, Methodology, Writing – review & editing, Writing – original draft, Conceptualization, Supervision, Project administration, Investigation, Data curation, Validation, Resources, Visualization, Funding acquisition.

Declaration of Competing Interest

The authors declare that they have no known competing financial interests or personal relationships that could have appeared to influence the work reported in this paper.

Acknowledgements

References

Abkar, E., Al-Nayili, A., Amiri, O., Ghanbari, M., Salavati-Niasari, M., 2021. Facile sonochemical method for preparation of Cs_2HgI_4 nanostructures as a promising visible-light photocatalyst. Ultrason. Sonochem. 80, 105827.

Aziz, K.H.H., Miessner, H., Mueller, S., Mahyar, A., Kalass, D., Moeller, D., Khorshid, I., Rashid, M.A.M., 2018. Comparative study on 2, 4-dichlorophenoxyacetic acid and 2, 4-dichlorophenol removal from aqueous solutions via ozonation, photocatalysis and non-thermal plasma using a planar falling film reactor. J. Hazard. Mater. 343, 107–115.

Balarabe, B.Y., Bowmik, S., Ghosh, A., Maity, P., 2022. Photocatalytic dye degradation by magnetic XFe_2O_3 (X: Co, Zn, Cr, Sr, Ni, Cu, Ba, Bi, and Mn) nanocomposites under visible light: A cost efficiency comparison. J. Magn. Magn. Mater. 562, 169823.

Bashir, A., Malik, L.A., Ahad, S., Manzoor, T., Bhat, M.A., Dar, G., Pandith, A.H., 2019. Removal of heavy metal ions from aqueous system by ion-exchange and biosorption methods. Environ. Chem. Lett. 17 (2), 729–754.

Bayat, S., Ghanbari, D., Salavati-Niasari, M., 2016. Pechini synthesis of Co_2SiO_4 magnetic nanoparticles and its application in photodegradation of azo dyes. J. Mol. Liq. 220, 223–231. https://doi.org/10.1016/j.molliq.2016.04.066.

Caglayan, C., Taslimi, P., Türk, C., Kandemir, F.M., Demir, Y., Gulcin, İ., 2019. Purification and characterization of the carbonic anhydrase enzyme from horse mackerel (Trachurus trachurus) muscle and the impact of some metal ions and pesticides on enzyme activity. Comp. Biochem. Physiol. C: Toxicol. Pharmacol. 226,. https://doi.org/10.1016/j.cbpc.2019.108605 108605.

Cao, R., Yang, H., Deng, X., Zhang, S., Xu, X., 2017. In-situ synthesis of amorphous silver silicate/carbonate composites for selective visible-light photocatalytic decomposition. Sci. Rep. 7 (1), 15001. https://doi.org/10.1038/s41598-017-15405-6.

Chen, S., Zhang, J., Zhang, C., Yue, Q., Li, Y., Li, C., 2010. Equilibrium and kinetic studies of methyl orange and methyl violet adsorption on activated carbon derived from Phragmites australis. Desalination 252 (1–3), 149–156.

Chiu, Y.-H., Chang, T.-F.-M., Chen, C.-Y., Sone, M., Hsu, Y.-J., 2019. Mechanistic insights into photodegradation of organic dyes using heterostructure photocatalysts. Catalysts 9 (5), 430.

Cui, Y., Wang, T., Liu, J., Hu, L., Nie, Q., Tan, Z., Yu, H., 2021. Enhanced solar photocatalytic degradation of nitric oxide using graphene quantum dots/bismuth tungstate composite catalysts. Chem. Eng. J. 420, 129595.

De Villiers, J.P., 1980. The crystal structure of braunite II and its relation to bixbyite and braunite. Am. Mineral. 65 (7–8), 756–765.

Deng, F., Min, L., Luo, X., Wu, S., Luo, S., 2013. Visible-light photocatalytic degradation performances and thermal stability due to the synergetic effect of TiO_2 with conductive copolymers of polyaniline and polypyrrole. Nanoscale 5 (18), 8703–8710.

Dheyab, M.A., Aziz, A.A., Jameel, M.S., Khaniabadi, P.M., Mehrdel, B., 2020. Mechanisms of effective gold shell on Fe_3O_4 core nanoparticles formation using sonochemistry method. Ultrason. Sonochem. 64, 104865.

Feng, Y., Yang, S., Xia, L., Wang, Z., Suo, N., Chen, H., Long, Y., Zhou, B., Yu, Y., 2019. In-situ ion exchange electrocatalysis biological coupling (i-IEEBC) for simultaneously enhanced degradation of organic pollutants and heavy metals in electroplating wastewater. J. Hazard. Mater. 364, 562–570.

Gautam, S., Agrawal, H., Thakur, M., Akbari, A., Sharda, H., Kaur, R., Amini, M., 2020. Metal oxides and metal organic frameworks for the photocatalytic degradation: A review. J. Environ. Chem. Eng. 8, (3) 103726.

Ghanbari, M., Salavati-Niasari, M., 2018. Tl_4CdI_6 nanostructures: facile sonochemical synthesis and photocatalytic activity for removal of organic dyes. Inorg. Chem. 57 (18), 11443–11455.

Ghanbari, M., Salavati-Niasari, M., 2021. Copper iodide decorated graphitic carbon nitride sheets with enhanced visible-light response for photocatalytic organic pollutant removal and antibacterial activities. Ecotoxicol. Environ. Saf. 208,. https://doi.org/10.1016/j.ecoenv.2020.111712 111712.

Guan, Y., Yu, H.-Y., Abdalkarim, S.Y.H., Wang, C., Tang, F., Marek, J., Chen, W.-L., Militky, J., Yao, J.-M., 2019. Green one-step synthesis of ZnO/cellulose nanocrystal hybrids with modulated morphologies and superfast absorption of cationic dyes. Int. J. Biol. Macromol. 132, 51–62.

Guo, W., Wang, Z., Wang, X., Wu, Y., 2021. General Design Concept for Single-Atom Catalysts toward Heterogeneous Catalysis. Adv. Mater. 33 (34), 2004287.

Haghjoo, H., Sangsefidi, F.S., Hashemizadeh, S.A., Salavati-Niasari, M., 2017a. Investigation the magnetic properties and the photocatalytic activity of synthesized Mn_7SiO_{12} nanostructures by green capping agent. J. Mol. Liq. 225, 290–295. https://doi.org/10.1016/j.molliq.2016.11.061.

Haghjoo, H., Sangsefidi, F.S., Salavati-Niasari, M., 2017b. Synthesis of $PbSiO_3$ nanoparticles in the presence of proteins as a greencapping agent and their application as photocatalyst. J. Mol. Liq. 247, 345–353. https://doi.org/10.1016/j.molliq.2017.10.029.

Haghjoo, H., Sangsefidi, F.S., Salavati-Niasari, M., 2018. Synthesis and characterization of Pb_2SiO_4 nanostructure: study of photocatalytic behavior of reactive Red198 and reactive Orange16 dyes as pollutants. J. Mater. Sci. Mater. Electron. 29 (10), 8002–8009. https://doi.org/10.1007/s10854-018-8806-9.

Hai, F.I., Yamamoto, K., Nakajima, F., Fukushi, K., 2008. Removal of structurally different dyes in submerged membrane fungi reactor—Biosorption/PAC-adsorption, membrane retention and biodegradation. J. Membr. Sci. 325 (1), 395–403.

Haider, S., Shar, S.S., Shakir, I., Agboola, P.O., 2022. Visible light active Cu-doped iron oxide for photocatalytic treatment of methylene blue. Ceram. Int. 48 (6), 7605–7612.

He, L., Li, M.-X., Chen, F., Yang, S.-S., Ding, J., Ding, L., Ren, N.-Q., 2021. Novel coagulation waste-based Fe-containing carbonaceous catalyst as peroxymonosulfate activator for pollutants degradation: Role of ROS and electron transfer pathway. J. Hazard. Mater. 417, 126113.

Huang, J.H., Rosén, E., 1994. Determination of Gibbs free energies of formation for the silicates MnSiO3, Mn2SiO4 and Mn7SiO12 in the temperature range 1000–1350 K by solid state emf measurements. Phys. Chem. Miner. 21 (4), 228–233. https://doi.org/10.1007/BF00202136.

Ikram, M., Hassan, J., Imran, M., Haider, J., Ul-Hamid, A., Shahzadi, I., Raza, A., Qumar, U., Ali, S., 2020a. 2D chemically exfoliated hexagonal boron nitride (hBN) nanosheets doped with Ni: synthesis, properties and catalytic application for the treatment of industrial wastewater. Appl. Nanosci. 10 (9), 3525–3528.

Ikram, M., Tabassum, R., Qumar, U., Ali, S., Ul-Hamid, A., Haider, A., Raza, A., Imran, M., 2020b. Promising performance of chemically exfoliated Zr-doped MoS 2 nanosheets for catalytic and antibacterial applications. RSC Adv. 10 (35), 20559–20571.

Ionescu, E., Linck, C., Fasel, C., Müller, M., Kleebe, H.J., Riedel, R., 2010. Polymer-Derived SiOC/ZrO2 Ceramic Nanocomposites with Excellent High-Temperature Stability. J. Am. Ceram. Soc. 93 (1), 241–250. https://doi.org/10.1111/j.1551-2916.2009.03395.x.

Kadam, A., Kim, T.G., Shin, D.S., Garadkar, K., Park, J., 2017. Morphological evolution of Cu doped ZnO for enhancement of photocatalytic activity. J. Alloy. Compd. 710, 102–113.

Karami, M., Ghanbari, M., Alshamsi, H.A., Rashki, S., Salavati-Niasari, M., 2021. Facile fabrication of Tl_4HgI_6 nanostructures as novel antibacterial and antibiofilm agents and photocatalysts in the degradation of organic pollutants. Inorg. Chem. Front. 8 (10), 2442–2460.

Khan, S.B., Ismail, M., Bakhsh, E.M., Asiri, A.M., 2022. Design of simple and efficient metal nanoparticles templated on ZnO-chitosan coated textile cotton towards the catalytic reduction of organic pollutants. J. Ind. Text. 51 (1_suppl), 1703S–1728S.

Kocyigit, U.M., Taslimi, P., Gulçin, İ., 2018. Characterization and inhibition effects of some metal ions on carbonic anhydrase enzyme from Kangal Akkaraman sheep. J. Biochem. Mol. Toxicol. 32 (8), e22172.

Konstantinou, I.K., Albanis, T.A., 2004. TiO2-assisted photocatalytic degradation of azo dyes in aqueous solution: kinetic and mechanistic investigations: a review. Appl Catal B 49 (1), 1–14.

Kucuk, M., Gulcin, İ., 2016. Purification and characterization of the carbonic anhydrase enzyme from Black Sea trout (Salmo trutta Labrax Coruhensis) kidney and inhibition effects of some metal ions on enzyme activity. Environ. Toxicol. Pharmacol. 44, 134–139. https://doi.org/10.1016/j.etap.2016.04.011.

Kumar, A., Pandey, G., 2017. A review on the factors affecting the photocatalytic degradation of hazardous materials. Material Science & Engineering International Journal 1 (3), 1–10.

Li, Z., Wang, G., Zhai, K., He, C., Li, Q., Guo, P., 2018. Methylene blue adsorption from aqueous solution by loofah sponge-based porous carbons. Colloids Surf A Physicochem Eng Asp 538, 28–35.

Liu, L., Wang, H., Wang, D., Li, Y., He, X., Zhang, H., Shen, J., 2020. ZnO@TiO2 Core/Shell Nanowire Arrays with Different Thickness of TiO2 Shell for Dye-Sensitized Solar Cells. Crystals 10 (4), 325 https://www.mdpi.com/2073-4352/10/4/325.

Maruthapandi, M., Saravanan, A., Manohar, P., Luong, J.H., Gedanken, A., 2021. Photocatalytic degradation of organic dyes and antimicrobial activities by polyaniline–nitrogen-doped carbon dot nanocomposite. Nanomaterials 11 (5), 1128.

Matos, J., Ocares-Riquelme, J., Poon, P.S., Montaña, R., García, X., Campos, K., Hernández-Garrido, J.C., Titirici, M.M., 2019. C-doped anatase TiO2: Adsorption kinetics and photocatalytic degradation of methylene blue and phenol, and correlations with DFT estimations. J. Colloid Interface Sci. 547, 14–29. https://doi.org/10.1016/j.jcis.2019.03.074.

Moshtaghi, S., Hamadanian, M., Amiri, O., Goli, M., Salavati-Niasari, M., 2021. Controllable synthesis and characterization of Mg2SiO4 nanostructures via a simple hydrothermal route using carboxylic acid as capping agent and their photocatalytic performance for photodegradation of azo dyes. RSC Adv. 11 (35), 21588–21599. https://doi.org/10.1039/d1ra02244j.

Naseem, K., Farooqi, Z.H., Begum, R., Wu, W., Irfan, A., Al-Sehemi, A.G., 2018. Silver nanoparticles engineered polystyrene-poly (n-isopropylmethacrylamide-acrylic acid) core shell hybrid polymer microgels for catalytic reduction of Congo red. Macromol. Chem. Phys. 219 (18), 1800211.

Nguyen, D.T.C., Le, H.T., Nguyen, T.T., Nguyen, T.T.T., Bach, L.G., Nguyen, T.D., Van Tran, T., 2021. Multifunctional ZnO nanoparticles bio-fabricated from Canna indica L. flowers for seed germination, adsorption, and photocatalytic degradation of organic dyes. J. Hazard. Mater. 420, 126586.

Rafiq, A., Ikram, M., Ali, S., Niaz, F., Khan, M., Khan, Q., Maqbool, M., 2021. Photocatalytic degradation of dyes using semiconductor photocatalysts to clean industrial water pollution. J. Ind. Eng. Chem. 97, 111–128.

Rahimzade, E., Ghanbari, M., Alshamsi, H.A., Karami, M., Baladi, M., Salavati-Niasari, M., 2021. Simple preparation of chitosan-coated thallium lead iodide nanostructures as a new visible-light photocatalyst in decolorization of organic contamination. J. Mol. Liq. 341,. https://doi.org/10.1016/j.molliq.2021.117299 117299.

Raza, A., Qumar, U., Hassan, J., Ikram, M., Ul-Hamid, A., Haider, J., Imran, M., Ali, S., 2020. A comparative study of dirac 2D materials, TMDCs and 2D insulators with regard to their structures and photocatalytic/sonophotocatalytic behavior. Appl. Nanosci. 10 (10), 3875–3899.

Salari, H., Kohantorabi, M., 2021. Heterogeneous photocatalytic degradation of organic pollutant in aqueous solutions by S-scheme heterojunction in nickel molybdate nanocomposites. J. Environ. Chem. Eng. 9, (5). https://doi.org/10.1016/j.jece.2021.105903 105903.

Salari, H., Zahiri, Z., 2022. Design of S-scheme 3D nickel molybdate/ AgBr nanocomposites: Tuning of the electronic band structure towards efficient interfacial photoinduced charge separation and remarkable photocatalytic activity. J. Photochem. Photobiol. A Chem. 426,. https://doi.org/10.1016/j.jphotochem.2021.113751 113751.

Sanakousar, F., Vidyasagar, C., Jiménez-Pérez, V., Prakash, K., 2022. Recent progress on visible-light-driven metal and non-metal doped ZnO nanostructures for photocatalytic degradation of organic pollutants. Mater. Sci. Semicond. Process. 140, 106390.

Şendal, K., Üstün Özgür, M., Gülen, J., 2022. Biosynthesis of ZnO photocatalyst and its application in photo catalytic degradation of methylene blue dyestuff. J. Dispers. Sci. Technol. 1–14. https://doi.org/10.1080/01932691.2022.2125005.

Sherin, L., Sohail, A., Mustafa, M., Jabeen, R., Ul-Hamid, A., 2020. Facile green synthesis of silver nanoparticles using Terminalia bellerica kernel extract for catalytic reduction of anthropogenic water pollutants. Colloid Interface Sci. Commun. 37, 100276.

Wahab, A., Imran, M., Ikram, M., Naz, M., Aqeel, M., Rafiq, A., Majeed, H., Ali, S., 2019. Dye degradation property of cobalt and manganese doped iron oxide nanoparticles. Appl. Nanosci. 9 (8), 1823–1832.

Wang, X., Guo, Y., Jia, Z., Ma, H., Liu, C., Liu, Z., Shi, Q., Ren, B., Li, L., Zhang, X., 2021. Fabrication of graphene oxide/polydopamine adsorptive membrane by stepwise in-situ growth for removal of rhodamine B from water. Desalination 516, 115220.

Wang, K., Qi, Z., Chen, Y., Chen, J., Yu, R., Wang, C., 2022. Hydrothermal synthesis of TiO2/BiOBr composites with enhanced photocatalytic activity. Therm. Sci. 26 (3 Part B), 2779–2785.

Wang, D., Wang, Y., Li, X., Luo, Q., An, J., Yue, J., 2008. Sunlight photocatalytic activity of polypyrrole–TiO2 nanocomposites prepared by 'in situ'method. Catal. Commun. 9 (6), 1162–1166.

Wang, L., Wu, J., 2021. A review of recent progress in silver silicate-based photocatalysts for organic pollutant degradation. Inorg. Chem. Commun. 129,. https://doi.org/10.1016/j.inoche.2021.108619 108619.

Wazir, M.B., Daud, M., Ali, F., Al-Harthi, M.A., 2020. Dendrimer assisted dye-removal: A critical review of adsorption and catalytic degradation for wastewater treatment. J. Mol. Liq. 315, 113775.

Wenten, I., Khoiruddin, K., Harimawan, A., Ting, Y., Boopathy, R., 2020. Membrane biosorption: recent advances and challenges. Current pollution reports 6 (2), 152–172.

Wu, S., Hu, H., Lin, Y., Zhang, J., Hu, Y.H., 2020. Visible light photocatalytic degradation of tetracycline over TiO2. Chem. Eng. J. 382, 122842.

Xiao, J., Liu, Q., Song, M., Li, X., Li, Q., Shang, J.K., 2021. Directing photocatalytic pathway to exceedingly high antibacterial activity in water by functionalizing holey ultrathin nanosheets of graphitic carbon nitride. Water Res. 198,. https://doi.org/10.1016/j.watres.2021.117125 117125.

Xu, S., Zhu, Y., Jiang, L., Dan, Y., 2010. Visible light induced photocatalytic degradation of methyl orange by polythiophene/TiO2 composite particles. Water Air Soil Pollut. 213 (1), 151–159.

Yang, M., Jin, H., Gui, R., 2023. Ag+-doped boron quantum dots with enhanced stability and fluorescence enabling versatile practicality in visual detection, sensing, imaging and photocatalytic degradation. J. Colloid Interface Sci. 639, 49–58. https://doi.org/10.1016/j.jcis.2023.02.066.

Yartasi, A., Çopur, M., Kocakerim, M., 1997. Dissolution kinetics of manganese ore in water saturated with sulphur dioxide. Chimica Acta Turcica-Istanbul- 25, 53–58.

Yousefzadeh, F., Yousif, Q.A., Ghanbari, M., Salavati-Niasari, M., 2022. Fabrication of TlSnI3/C3N4 nanocomposites for enhanced photodegradation of toxic contaminants below visible light and investigation of kinetic and mechanism of photocatalytic reaction. J. Mol. Liq. 118443.

Zhang, Y., Li, K., Liao, J., 2020. Facile synthesis of reduced-graphene-oxide/rare-earth-metal-oxide aerogels as a highly efficient adsorbent for Rhodamine-B. Appl. Surf. Sci. 504,. https://doi.org/10.1016/j.apsusc.2019.144377 144377.

Zhang, H., Xue, G., Chen, H., Li, X., 2018a. Magnetic biochar catalyst derived from biological sludge and ferric sludge using hydrothermal carbonization: preparation, characterization and its circulation in Fenton process for dyeing wastewater treatment. Chemosphere 191, 64–71.

Zhang, X., Yan, K., Song, Y., Wang, Z., Wu, J., Yu, D., 2018b. Preparation of Ag3PO4/AgBr Hybrids Using a Facile Grinding Method and Their Applications as Photocatalysts. Chem. Res. Chin. Univ. 34 (4), 649–654. https://doi.org/10.1007/s40242-018-7363-3.

Zhou, Y., Lu, J., Zhou, Y., Liu, Y., 2019. Recent advances for dyes removal using novel adsorbents: a review. Environ. Pollut. 252, 352–365.

Zhuang, Y., Zhu, Q., Li, G., Wang, Z., Zhan, P., Ren, C., Si, Z., Li, S., Cai, D., Qin, P., 2022. Photocatalytic degradation of organic dyes using covalent triazine-based framework. Mater. Res. Bull. 146, 111619.